Materials Advances

ROYAL SOCIETY OF CHEMISTRY

PAPER

View Article Online
View Journal | View Issue

Cite this: *Mater. Adv.*, 2025, **6**, 1988

Fabrication of a mesoporous $CoFe_2O_4$/rGO nanohybrid and laccase interface biosensor for rapid detection of adrenaline for neurodegenerative disease diagnosis†

Rahul Verma,‡ Surendra K. Yadav,‡ Diksha Singh and Jay Singh *

Received 9th December 2024,
Accepted 12th February 2025

DOI: 10.1039/d4ma01216j

rsc.li/materials-advances

A hydrothermally synthesized mesoporous $CoFe_2O_4$ (CF)/reduced graphene oxide (rGO) nanohybrid (nh) provides the electroactive surfaces and facilitates fast electron transfer between the nanofabricated bioelectrode–electrolyte interfaces, responsible for the high electrocatalytic activity in sensing adrenaline (AD). A promising biosensor for detecting adrenaline and bovine serum albumin (BSA) used as a real sample for diagnosing neurodegenerative diseases is described here. This study focuses on the electrochemical impedance biosensing of AD because of its unique ability to identify various kinds of health issues, including blood pressure, fight-or-flight response, memory loss, multiple sclerosis, Parkinson's disease, and cardiac asthma. A La/CF/rGO/ITO bioelectrode (La: Laccase) is the biosensor component. It is created by electrophoretic deposition (EPD) of a CF/rGO nh and drop-casting immobilization of the La-enzyme. The low charge-transfer resistance (R_{ct}) of the CF/rGO electrode was sensed by electrochemical impedance spectroscopy (EIS), confirming the synergistic impact of CF/rGO on the La/CF/rGO/ITO fabricated bioelectrode in AD detection. This gives the high heterogeneous rate constant (K_s: 2.83 × 10^{-4}) and increases the surface adsorption and diffusion coefficient (D: 5.25 × 10^{-2} cm^2 s^{-1}). The proposed biosensor exhibited high sensitivity (0.214 Ω μM^{-1} cm^{-2}), long linear range (1 to 500 μM), lower detection limit (LoD: 40.3 μM), high selectivity (RSD 5.8%), and stability with good recovery %, emphasizing its potential implementation in biosensing techniques for monitoring neurotransmitter disorders in real world applications.

Introduction

The neurotransmitter (NT), hormone, and prescription drug adrenaline (AD) is an important member of the catecholamine family. The adrenal medulla and sympathetic nerve (endocrine systems) release AD. It is also an important metabolic biological fluid and natural NT organic compound found in the central nervous system, and is used as a chemical messenger to facilitate vasoconstriction, cardiac stimulation, and blood sugar levels.[1,2] It is also important for treating anaphylaxis,[3] acute asthma, alleviating bronchiolitis, hypertension, and cardiac arrest,[4] used as a drug, and associated with physiological activities to trigger the sympathetic nervous system's fight-or-flight response, increasing heart rate, and expanding the lungs.[5] Catecholamines are important in the development of neurological disorders like Parkinson's disease, multiple sclerosis, and Alzheimer's disorder. Normal body fluids typically contain concentrations of these chemicals in the nM and pM range, which are linked to diseases like hypoglycemia, high blood pressure, stress, memory loss, and thyroid hormone disorders.[6–9] It also promotes the production of sugar from food in the body, enables faster breathing, and dilates pupils.[10] In 2007, the World Health Organization revealed that public health challenges due to neurological disorders affect around one billion people in the world, significantly 50 million due to epilepsy, 24 million due to Alzheimer's disease and dementias, and each year 6.8 million die from neurological disorders.[11] Sensitive and selective monitoring with high efficiency and accuracy in real-life samples is extremely desirable, as NTs are crucial for pathological research.[12] The analytical methods on offer can assess and diagnose patients, but they have significant drawbacks as they take a lot of time, and require the support of scientists in the laboratory. As science and technology have advanced quickly, so has the desire for personalized treatment plans and monitoring techniques. Such scientific diagnostic tool might become part of newly developed analysis techniques. Researchers are currently attempting to create analytical processes that are quicker, more accessible, have short-time processes, are eco-friendly, and miniaturized.[13] In the last few decades many

Department of Chemistry, Institute of Science, Banaras Hindu University, Varanasi, 221005, Uttar Pradesh, India. E-mail: jaysingh.chem@bhu.ac.in, jaimnnit@gmail.com; Tel: +91-9871766453

† Electronic supplementary information (ESI) available. See DOI: https://doi.org/10.1039/d4ma01216j

‡ These authors contributed equally.

techniques have been applied such as photoluminescence, colorimetric analysis,[14,15] high-performance liquid chromatography,[16] spectrophotometric,[17] and electrochemical analysis techniques.[18,19] Since AD is an electrochemically active bio-analyte, its physiological and neurochemical systems are electrochemically valuable targets for determining both its qualitative and quantitative levels. These systems should also be readily available to users who demand high levels of sensitivity, selectivity, and affordability in their detection methods. Electrochemical sensors have a promising scientific future from an analytical perspective due to their high sensitivity, quick responses, ease of control, and real-time and accurate detection.[19,20] Strategically speaking, a biosensor based on electrochemical impedance spectroscopy (EIS) has exciting scientific potential; with science and technology advancing at a rapid rate, a newly created analytical process is required to be utilized as a scientific diagnostic device.

The scientific and engineering communities have been drawn to graphene, a remarkable 2D sp2 – hybridized carbon material, because of its unique qualities, such as large surface area, mechanical strength, thermal stability, ultra-thin nanostructure, and excellent electrical conductivity (faster carrier mobility). Graphene has become attractive as an electrode material for use in electrochemical applications, like sensors/biosensors, supercapacitors, and catalysis with promising potential applications.[21–23] Graphene sheets have finite dimensions and morphological characteristics such as dislocation, edge defects, and rings with five to eight members that resemble hexagons and honeycombs, attached *via* van der Waals and π–π weak interactions. Reduced graphene oxide (rGO) and graphene oxide (GO) are two significant derivatives of graphene. rGO exhibits increased electrical conductivity because of the removal of oxygen-holding carboxyl groups (COOH) present on the basal plane and edges of the crystal lattices. The significance of rGO focused on in this article is special characteristics like its optical, mechanical, thermal, surface area, and electrical characteristics which have extensive usefulness such as in photocatalysts,[24] energy storage, catalysis, solar cells,[25] biosensors/sensors,[26] hybrid materials, and electronic devices as ideal materials for electrochemical applications.[27,28] Furthermore, superior dispersibility and hydrophilicity in aqueous media mainly depend on groups such as COOH, OH, and the epoxy moiety on the surface of rGO.[29,30] However, these groups on the surface of rGO also limit its electrical conductivity, which makes it difficult to directly use rGO in electrode materials and devices. As a result, to facilitate its direct deployment, the topic of restricted electrical conductivity in rGO needs attention. The goal of recent research has been to understand better how to improve rGO electro-conductive capabilities for a range of analytes by incorporating metal/ferrite oxide hybrid materials by enhancing the rGO electrical conductivity to utilize the mixed nh (Ferrites) materials in several electrode material and electronic device applications.[31,32] Thus, using techniques like doping, chemical modification, and nh synthesis with other materials has been enhancing the electrocatalysis of rGO.[33–35]

Nanoparticles (NPs) of transition metal oxides have emerged with fascinating potential for a range of potential applications like water purification, energy conversion, fuel cells, sensors, and storage.[36] Because of these NPs' redox activity, nontoxicity, high stability, affordability, environmentally friendly nature, and natural abundance, researchers studying electrocatalysis have been keenly interested in them.[37–39] However, individual metal oxides' poor conductivity has restricted their practical application. The use of mixed transition metal oxide NPs has been investigated as a solution to this constraint. Because these NPs combine two distinct metal species into one crystal structure, they have mixed valency and can facilitate a variety of redox processes.[36] Additionally, by combining these mixed metal oxides with pure metal oxides in a synergistic way, the effectiveness of the electrocatalytic reaction can be improved, leading to a wider range of working potentials, better conductivity, more electroactive sites, and increased stability. Because of their improved physical and chemical qualities over traditional bulk materials, magnetic NPs have been trendsetting in recent years.[40–42] Ferrites are a class of magnetic NP materials with significant technological value and a wide range of applications, including biosensing.[19,43] To monitor neurotransmitters and epinephrine concurrently using an electrochemical approach, Roychoudhury *et al.* used the NiO/rGO platform.[44] Therefore, in the electrochemical monitoring of bio-analytes, the combination of CF and rGO offers promising candidates with exceptional catalytic and conductive efficiency.

After applying the produced nanohybrid (nh) to the ITO surface, the modified CF/rGO/ITO electrode is subjected to the drop-cast approach to optimize the immobilization of the laccase (La) enzyme. Because of the many active sites and efficient, fast electron transport mechanisms in the mesoporous CF/rGO nh on modified ITO (La/CF/rGO/ITO), enhanced sensing signals can be generated to evaluate AD selectively. Compared to the CF/ITO pretreatment, the CF/rGO-modified electrode shows a larger effective surface area and electrocatalytic efficiency in favor of AD. We conclude that the CF/rGO nh is a promising material for biosensing applications using electrochemical techniques. Based on our knowledge, no earlier report was found on novel La/CF/rGO/ITO bioelectrodes for AD monitoring by EIS techniques. The low-temperature hydrothermally synthesized CF/rGO nh are electrophoretically deposited and enzyme immobilized on their surface to investigate the AD selectively, enhancing the active sites with surface area for binding and fast charge transfer reaction. In addition, the fabricated bioelectrode detects the AD with a more extended linear range, lower detection limit (LoD), stability, and high sensitivity and was applied to the real (BSA) sample with relative standard deviations (RSD 8.3%) recorded. These results make the CF/rGO unique compared to traditional materials that offer several advantages in monitoring neurotransmitters important to neurological disorders and healthcare monitoring.

Experimental optimization

Chemicals and reagents

The salts of $Fe(NO_3)_3{\cdot}9H_2O$, $Co(NO_3)_2{\cdot}6H_2O$, (~99% purity) NH_3 (25% solution), and H_2O_2 30% solution were procured from Merck Mumbai, India. Graphite flakes, H_2SO_4 (98% pure),

([NaH_2PO_4]·$2H_2O$), and ([Na_2HPO_4]·$2H_2O$), (99% pure) were purchased from Sigma-Aldrich, and $K_3[Fe(CN)_6]$, and $K_4[Fe(CN)_6]\cdot 3H_2O$, (98.5% pure) are procured from Merck Mumbai. Adrenaline hydrochloride [formula $C_9H_{13}NO_3$·HCl], an enzyme extracted from *Agaricus bisporus*, a deep brown powder (≥4 units per mg solid powder) laccase (La), and NaCl (99%) and ITO, used as working electrodes (20 Ω sq^{-1} resistivity), were procured from Sigma-Aldrich.

Synthesis of CF/rGO nanohybrid and GO

Using the Hummers' method[45] can produce GO by using graphite flakes. In 46 mL of H_2SO_4 solution, 2 gm of graphite flakes were mixed with the slow addition of 6 gm of potassium permanganate at 0–50 °C for 2 h continuous stirring. The mixed solution was heated at 35 °C for 12 h, with the addition of 25 ml H_2O_2 solution and 92 ml of distilled water to obtain a yellowish color solution. The solution was centrifuged, splashed with MilliQ water multiple times, and dried to produce GO/rGO, which was confirmed by spectroscopic techniques, to be utilized in various applications.

Mesoporous cobalt ferrite NPs were hydrothermally synthesized from salts of $Co(NO_3)_2\cdot 6H_2O$ (0.4 M aqueous solution) and $Fe(NO_3)_3\cdot 9H_2O$ (0.8 M aqueous solution) as precursors (1 : 2 ratio of concentration) in 50 ml solution, while stirring for 2 h (1200 rpm) at 60 °C. After that, 100 mg GO sheets were used to prepare a solution in 25 ml distilled water after 35 minutes of ultrasonication. Then, the GO solution and salt solution were mixed for 2 h with the same stirring speed, and the pH of the solution was found to be five. In the later step, the NH_3 solution of 25% was added, with surfactant oleic acid (2 ml, for nucleation and high crystallinity); the pH reached up to 9 to start the conversion from nitrate salt solution to metal hydroxide (Fe/Co–OH) solution at 60 °C and with stirring for 3 h. In addition, the mixture of the blackish solution was placed in Teflon-lined stainless auto-clave vessels (100 ml) and synthesized at 180 °C for 20 h. After completing the hydrothermal reactions, the autoclave was cooled, the solution was centrifuged in a water/ethanol mixture, dried at 90 °C overnight, and then calcined at 400 °C for 6 h. The resulting powder was confirmed by XRD and Raman analysis as a CF/rGO nh,[46] and a schematic presentation of the hydrothermal synthesis is represented in Scheme S1 (ESI†). An equivalent approach was also applied in the preparation of CF NPs using a hydrothermal method without the addition of GO in the reaction conditions, and these prepared mesoporous CF/rGO nh materials were used to fabricate electrodes for electrochemical monitoring of AD neurotransmitters.

Results and discussion

The X-ray diffraction (XRD) patterns of the rGO, CF, and CF/rGO mesoporous nh were used to investigate their crystallinity and phase purity. Fig. 1A shows the XRD results obtained with CuKα radiation at 1.5418 Å and scanning angles from 10 to 90° (2θ) at a 2° min^{-1} scan rate (X-ray D8 Advance Diffractometer, Bruker). The XRD spectrum at 2θ angles of ∼18.1, 29.8, 35.2, 42.9, 53.3, 56.8, and 62.5 correspond to the (111), (220), (311), (400), (422), (511), and (440) planes of the CF/rGO nh, respectively. This result is similar to standard data on CF's face-centered cubic spinel ferrite structure (JCPDS No. 030864). Additionally, the peak corresponding to the 002 plane at 26.1° (2θ) confirmed the presence of rGO, and this peak was also seen in the nh XRD spectra. The peaks of CF and rGO were observed in the nh XRD spectra, confirming the CF/rGO *in situ* low-temperature synthesized nh. The lattice constants (a) of CF/rGO nh were calculated by using eqn (1) and found to be 8.4 Å, which agrees well with the standard lattice constant (8.3 Å). The average crystallite size (D) values were evaluated by using Scherrer's[47] eqn (2) to calculate the crystallite size as 14 nm. Furthermore, the proposed nh's lattice density (ρ) was assessed using eqn (3), and was found to be 5.17 g cm^{-3}.

$$a = \lambda\,(h^2 + k^2 + l^2)^{1/2}/2\sin\theta \quad (1)$$

$$D = 0.9\lambda/\beta\cos\theta \quad (2)$$

$$\rho = nM/N_A a^3 \quad (3)$$

The λ is the wavelength of the X-ray, the miller indices are h, k, and l of the plane (311 planes of high intensity), θ is the Bragg diffraction angle in radians, β is the full width at half maximum (FWHM) in radians, n is the number of atoms/molecules (8 in spinel) participating in the lattice structure, M is the molecular weight of the prepared materials, and N_A is Avogadro's number (6.02×10^{23} mol^{-1}).

The XRD peak broadening is a consequence of lattice strain and small particle size. This principle underpins several techniques, including the Scherrer equation, Hall–Williamson method, and the Warren–Averbach method. In this study, the Hall–Williamson method was used to estimate lattice strains, eqn (S1) (ESI†). Fig. S1(A and B) (ESI†) shows a positive slope of the strain curve for CF/rGO (0.00097) and CF (0.00159) indicating the presence of tensile strain in the lattice. As a result, both lattice strain and the observed Debye–Waller factor increase. Debye temperatures are calculated using the zero-strain values of the Debye–Waller factor.[48] The Debye temperature (T_D) varies as a function of the band gap (E_g) of the material, following the relationship $T_D \propto \exp(E_g)$.[49] Consistent with this trend, the tensile strain in CF is greater than that in CF/rGO, leading to a larger band gap (calculated band gap value from UV-vis data) and, consequently, is well-aligned with the CV curve as well.

The local distortion and cation distribution can be determined using Raman spectroscopy. The spinel of rGO, CF, and CF/rGO nh is shown in Fig. 1B, revealing a sharp and intense absorption band signifying their high crystallinity. High-performance charged coupled device detectors (Horiba LabRam HR evolution spectrometer) use a 633 nm He–Ne beam illuminating the sample in the 200–3500 cm^{-1} range. The inverse spinel structured materials have Co^{2+} cation occupying the octahedral (O_h) sites and Fe^{3+} cations in half of the O_h sites and half of the tetrahedral (T_d) sites. Furthermore, the CF has a cubic face-centered structure containing space group $Fd\bar{3}m$, and 56 atoms

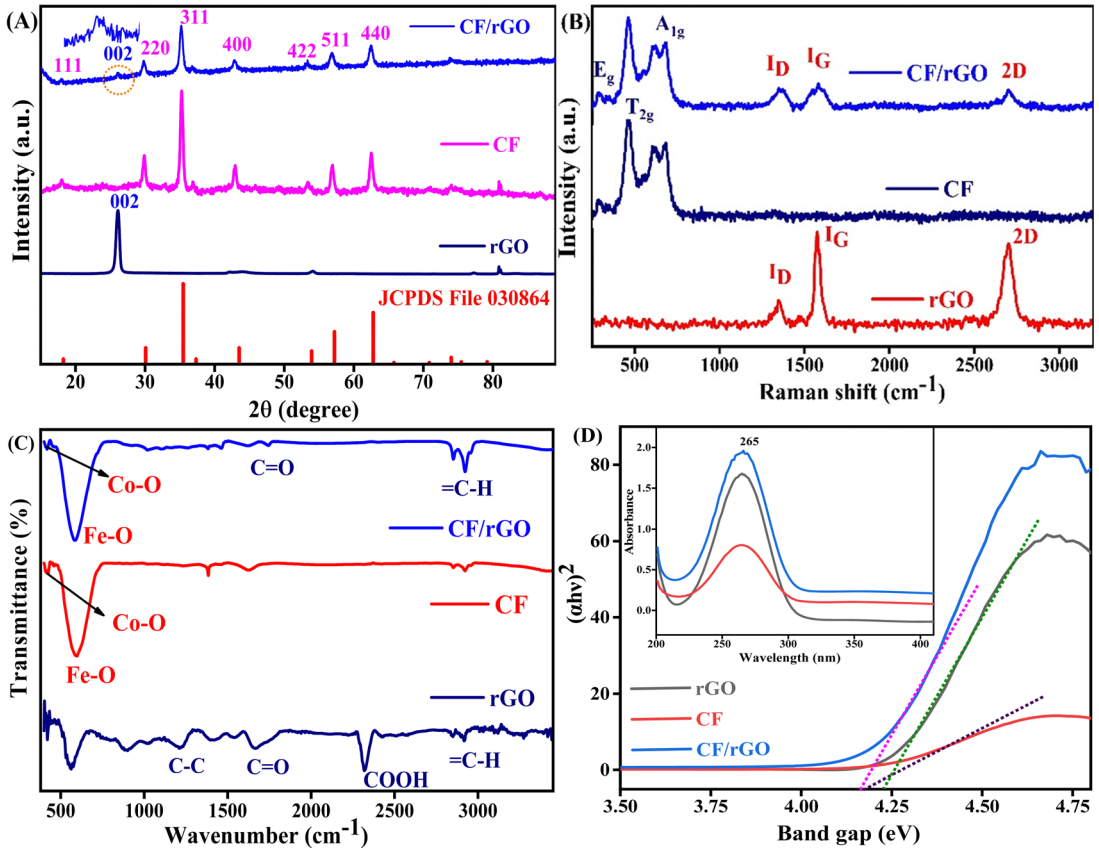

Fig. 1 (A) The XRD graph of rGO, CF, and CF/rGO nh with an equivalent plane, (B) Raman active modes of rGO, CF, and CF/rGO in nondestructive Raman scattering, (C) functional groups of rGO, CF, and CF/rGO nh in FTIR spectra, (D) UV-vis spectra of rGO, CF, and CF/rGO nh (inset), and the equivalent Tauc plot for band gap calculation.

(Z = 8) in one complete unit cell[50] analysis to predict the spinel modes;

$$\Gamma = E_g\,(R) + A_{1g}\,(R) + T_{1g} + 3T_{2g}\,(R) + 2A_{2u} + 2E_u + 4T_{1u}\,(IR) + 2T_{2u}$$

where T_{1u} modes are IR active modes, T_{1g}, A_{2u}, E_u, and T_{2u} represent the silent modes, and E_g, A_{1g}, and T_{2g} are Raman active modes.[47] The spectrum of CF showed two strong bands at 468 and 680 cm^{-1} and two weaker bands around 290 and 616 cm^{-1}. The higher frequency peaks at 616 and 680 cm^{-1} are linked with the basic A_{1g} symmetric modes, involving the stretching mode of oxygen atoms in the T_d lattice site. However, the lower frequency bands at 290 (E_g) and 468 (T_{2g}) cm^{-1} modes due to bending of the oxygen atom in the M–O bond at the OH site by symmetric and antisymmetric modes present in crystalline spinel CF NPs were confirmed by group theory.[51] The two bands recognized as D (1350 cm^{-1}), obtained due to the presence of defect-induced vibrations of the carbon atoms in the hexagonal lattice with A_{1g} symmetry, and G bands (1580 cm^{-1}) are related to symmetric sp^2-hybridized carbon atoms with E_{2g} symmetry in the graphitic domains of the in-plane stretching mode.[52] The intensity ratio of the D to G band (I_D/I_G) provides information about the degree of graphitization, intensity, shape, and position of the band depending on the layers in the GO and the band's size. Additionally, the 2D band associated with the second order two phonon mode at 2700 cm^{-1} is due to the inelastic scattering of two phonons with opposite momentum in the pure rGO spectrum. Thus, these results of Raman analysis approve the formation of CF/rGO nh and justify the outcome of XRD analysis.

Fourier-transform infrared (FTIR) spectroscopy reveals the functionalization and location of surface groups in CF and CF/rGO nh detected in the range of 400 to 3500 cm^{-1} (JASCO-FTIR-4700). Fig. 1C shows the vibrational bands between 420 cm^{-1} to 580 cm^{-1} are related to the T_d (Co–O) and O_h (Fe–O) rearrangement of cation sites respectively, to confirm the formation of inverse spinel ferrite.[20] The stretching mode of symmetric and antisymmetric peaks of C–H at 2900–2950 indicates the polymer matrix rGO with 1220 (C–C), 1670 (C═O), and 2320 (COOH) peaks containing functional groups.[43] The carbonyl group, epoxy, and carboxylic groups confirm the formation of CF/rGO nh, supporting the final results of the XRD analysis.

The optical behavior of rGO, CF, and CF/rGO nh was inspected by UV-vis absorption spectroscopy from 200 to 400 nm wavelength (UV-1700 pharma Spec, SHIMADZU, D_2, and W lamp). Fig. 1D shows that the absorption spectra of the hydrothermally prepared rGO, CF, CF/rGO nh is ∼265 nm. Furthermore, these results are utilized to calculate the change in the samples' energy gap (band gap E_g) by using the Tauc relationship,[53] which is given in eqn (4).

$$\alpha = K(h\nu - E_g)^n/h\nu \quad (4)$$

Here α is the absorption coefficient, K is a constant ($K \sim 1$), $h\nu$ is the photon energy ($h\nu$ = 1240 eV), and n is the direct transition in the semiconductor (1/2). The plot of $(\alpha h\nu)^2$ *versus* $h\nu$ is used to determine the direct band gap of the proposed materials. Thus, the rGO, CF, and CF/rGO nh have direct optical band gaps of 4.22, 4.16, and 4.07 eV, respectively, after Tauc plot analysis. These results reveal that the rGO addition in the nh decreases the electron–hole band gap and enhances the charge transfer activity of the CF/rGO nh. Thus, the lower energy gap in nh materials caused the insulators to exhibit semiconductor behaviors, which enhances their electrical conductivity and allows them to be utilized in electrochemical biosensing applications.[54]

High-resolution (HR) TEM observations were performed to examine the internal shape, morphology, and crystalline nature of the mesoporous CF and CF/rGO nh. Fig. 2A depicts the CF magnetic spinel ferrite achieving a uniform rectangular and rhombus mix-phase parallelogram morphology. Furthermore, the investigation of lattice fringes in CF is seen in the HR-TEM image, Fig. 2B. The JCPDS file confirms lattice spacing (0.25 nm) equivalent to the high-intensity plane (311). Thus, the SAED pattern of CF indexed (Fig. 2C), which is like the Debye–Scherrer pattern of CF indexed (620, 511, 422, and 220) planes, confirms the polycrystalline nature of the materials. The CF/rGO nh HR-TEM images show the spherical as well as rectangular morphology and lattice plane, also showing *d*-spacing (0.25 nm) equivalent to the high intensity 311 plane, and the similar spacing circular SAED pattern confirms the polycrystalline nature of the nh material (Fig. 2D–F). The CF and CF/rGO nh average particle sizes calculated by applying the Lorentzian function in the Image-J software were found to be 21 nm and 19.5 nm, respectively. Relative to lattice fringes in HRTEM images, the dominant plane in XRD *d*-spacing confirms the high crystallinity of the proposed materials applied for electrochemical analysis.

The surface micrograph of the proposed materials is evaluated by scanning electron microscopy (SEM) (model: ZEISS, EVO-18, and LaB6 electron source). Fig. 3A and B represent the SEM micrograph of CF, which are spherical agglomerated uniform particles and corresponding energy dispersive X-ray (EDX) profiles with elements' atomic percentages to confirm the prepared materials are CF NPs. In Fig. 3C, the addition of rGO in the CF decreases the agglomeration of spherical NPs due to the rGO sheet distributed between the CF NPs and prevents aggregation. In addition, the nh formed a large void of great benefit in the reaction interface. The output obtained thus validates the intercalation of CF on the rGO surface to increase the specific surface area (which is further validated by BET analysis in Fig. 4B) for use in electrochemical biosensing applications. The EDX analysis and composition of elements present in the prepared nanohybrid material are shown in Fig. 3D. The nh material exhibits the atomic percentages of the components Co, Fe, O, and C to prove the composition of the synthesized materials and support the XRD and Raman findings highlighting the presence of CF/rGO nh.

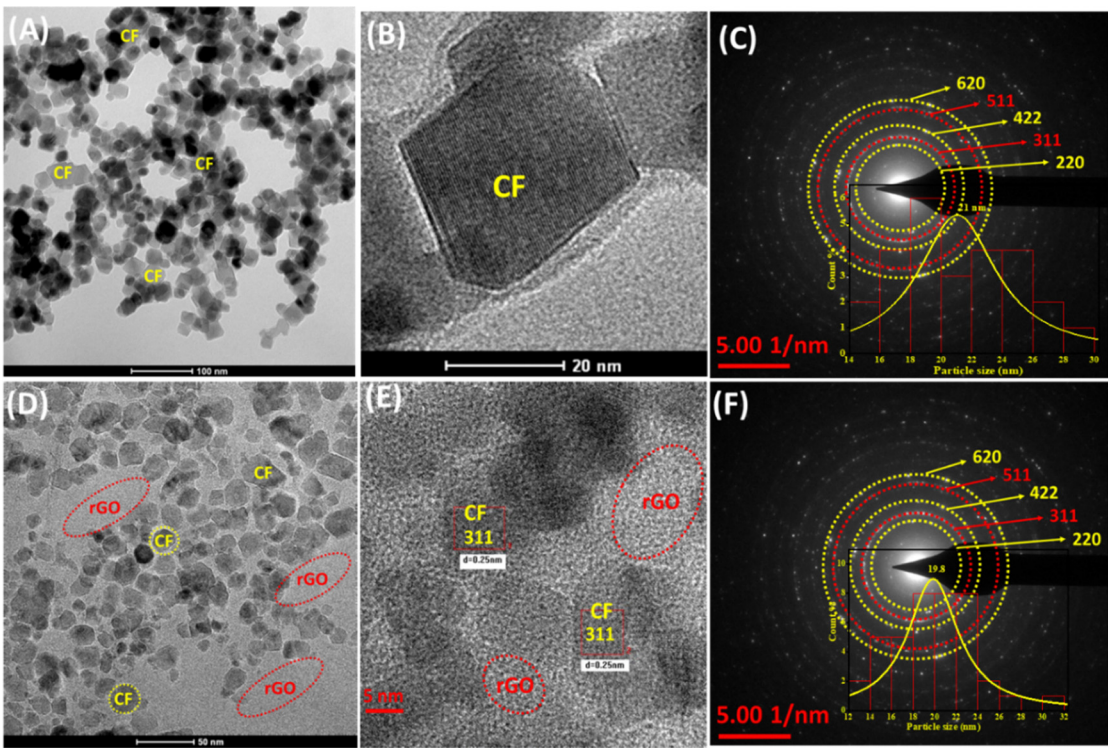

Fig. 2 (A) and (B) HR-TEM microimages of CF with rectangular morphology, (C) SAED pattern of CF with equivalent planes confirmed by JCPDS *d*-spacing value, and the inset histogram shows the average particle size, (D) and (E) HR-TEM microimages of mesoporous CF/rGO nh indicating lattice fringes equivalent to high-intensity planes, and (F) the SAED pattern of mesoporous CF/rGO nh with equivalent planes confirmed by JCPDS *d*-spacing and average particle size histogram.

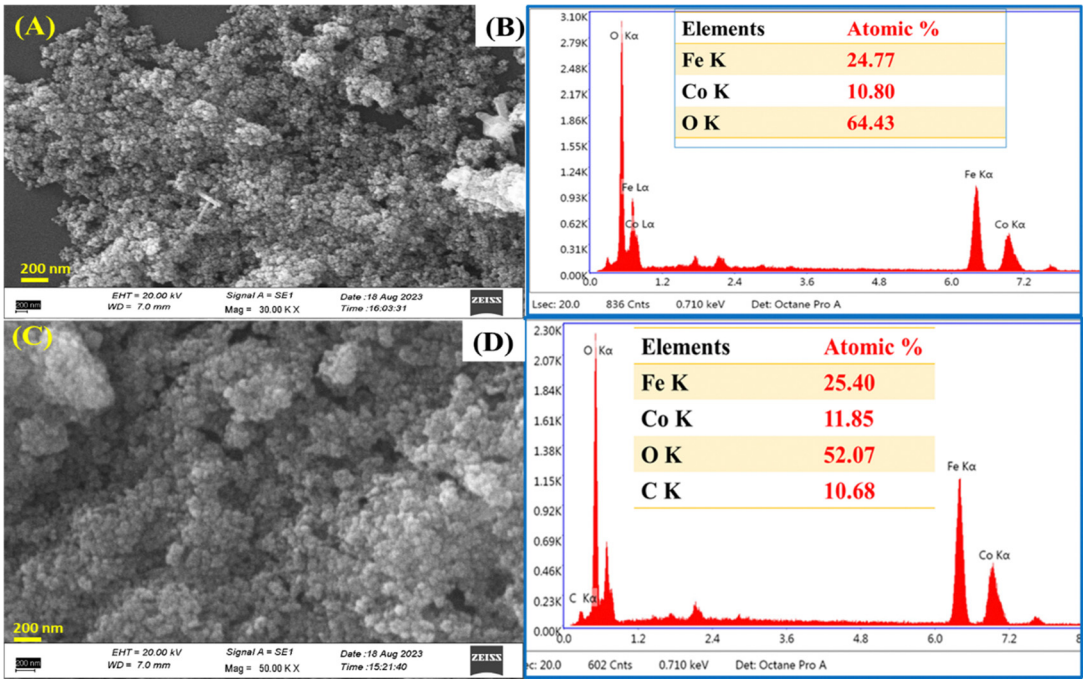

Fig. 3 (A) and (B) SEM micrograph of CF with EDX containing the corresponding element percentages, and (C) and (D) SEM micrograph of CF/rGO with EDX containing the corresponding element percentages.

Furthermore, the atomic force microscopy (AFM) analysis tapping mode was used to analyze the surface features of the CF and CF/rGO thin film on the ITO surface. Fig. S2(A and B) (ESI†) shows that the CF average roughness (S_a) is 6.3 nm, root mean square roughness (S_q) is 8.1 nm and maximum area peak height (S_p) is 33.2 nm, and Fig. S2(C and D) shows the roughness parameters of CF/rGO such as S_a is 4.3 nm, S_q is 5.6 nm, and S_p is 25.9 nm, which are discussed in the ESI† (Section 2).

The key factors that affect the charge/ion transport in electrochemical analysis are the surface area, porosity, and pore size allocation. The larger the specific surface area and hierarchical pores the greater the number of active sites for electrochemical reactions. N_2 adsorption porosimetry is frequently employed in experimental settings to characterize the specific surface area (in $m^2\ g^{-1}$), pore size allocation, and open porosity of mesoporous materials (pore size 2 to 50 nm in range). The specific surface area of the mesoporous materials is determined by using the Brunauer–Emmett–Teller (BET) method expressed as:

$$\text{BET} = N_m N_A C_{N_2}$$

where N_A is Avogadro's number (in mol^{-1}), and C_{N_2} is the cross-sectional area of an N_2 molecule adsorbed on the surface as a monolayer (in m^2). Additionally, N_m is a measure of the monolayer capacity (in mol g^{-1}), specified as the amount of N_2 required to form a monolayer over the surface of the pores in one gram of the porous nh material. The adsorption–desorption N_2-isotherm mesoporous behavior of CF and CF/rGO nh is shown in Fig. 4A and B (Model As-i Q-C) (P/N: 62143-iTCD), Quantachrome surface area and pore size analyzer). According to the IUPAC, the CF NPs have a type IV adsorption indicating the mesoporous nature of the materials with a hysteresis loop between 0.65–1.0 relative pressure, signifying the bimodal porous nature of the NP-containing multilayer adsorption.[55] Additionally, the type-IV isotherm of the mesoporous CF/rGO nh exhibits a significant hysteresis loop, indicating the formation of slit-like pores.[56] The reason for this mesoporous structure may be the attachment of CF NPs in the inter-layers of the rGO sheet. The BET-specific surface area of CF and CF/rGO is 53.15 and 119.2 $m^2\ g^{-1}$, the average pore radius is 32.6 and 87.4 Å, and the total pore volume is 0.095 and 0.72 cc g^{-1}, respectively. Thus, the increased specific surface area of the mesoporous CF/rGO nh suggests that the CF NP is evenly dispersed on the rGO matrix or between the rGO layers, creating pores in the nh. The larger surface area is effectively involved in adsorption, diffusion, and interaction with enzyme biomolecules to enhance the reactions' catalytic activity. As a result, the bioelectrode and electrolyte interface enhances the conductivity of the nh with pore-radius, and better penetration of electrolytes through nano-channels enhances the electrochemical performance in mesoporous nh materials.

X-ray photoelectron spectroscopy (XPS) was carried out on the electrostatically self-assembled CF and CF/rGO nh to confirm the elemental oxidation states, binding energy, and surface composition. The elements Co, Fe, O, and C were detected in the CF/rGO nh, which are excited by X-ray at the adjustable spot size from 10 to 200 μm, up to 1.4 mm scanning dimensions (ULVAC-PHI, INC.PHI 5000 Versa Probe-III, X-ray source AlKα, $h\nu$ = 1486.6 eV) as shown by the survey spectrum illustrated in Fig. 5A. These elements were evidence of the

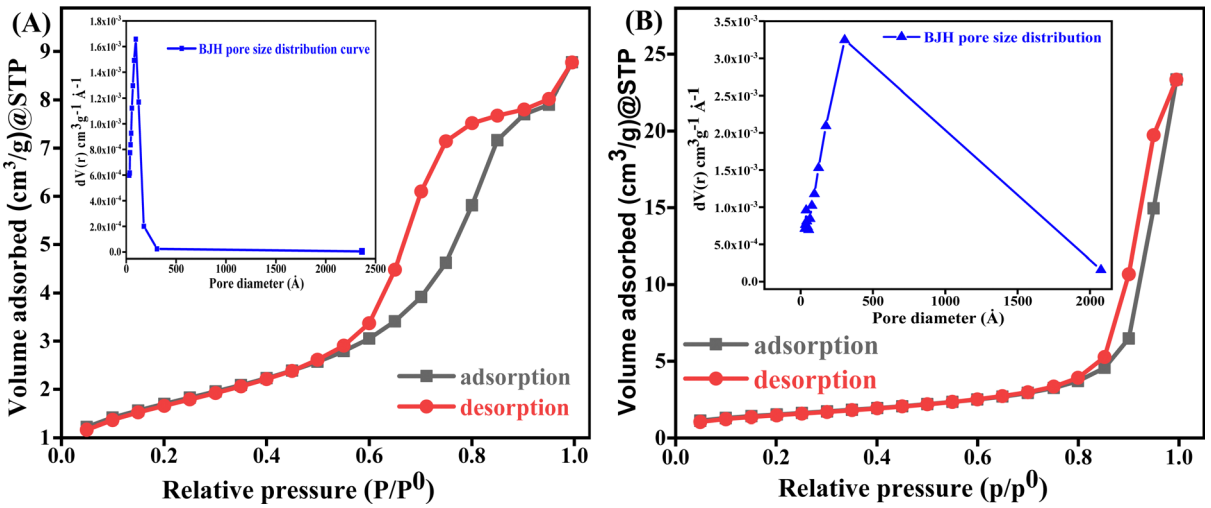

Fig. 4 (A) The mesoporous CF and pore diameter, and (B) the mesoporous CF/rGO nh with a pore diameter of BET adsorption–desorption N_2 isotherm.

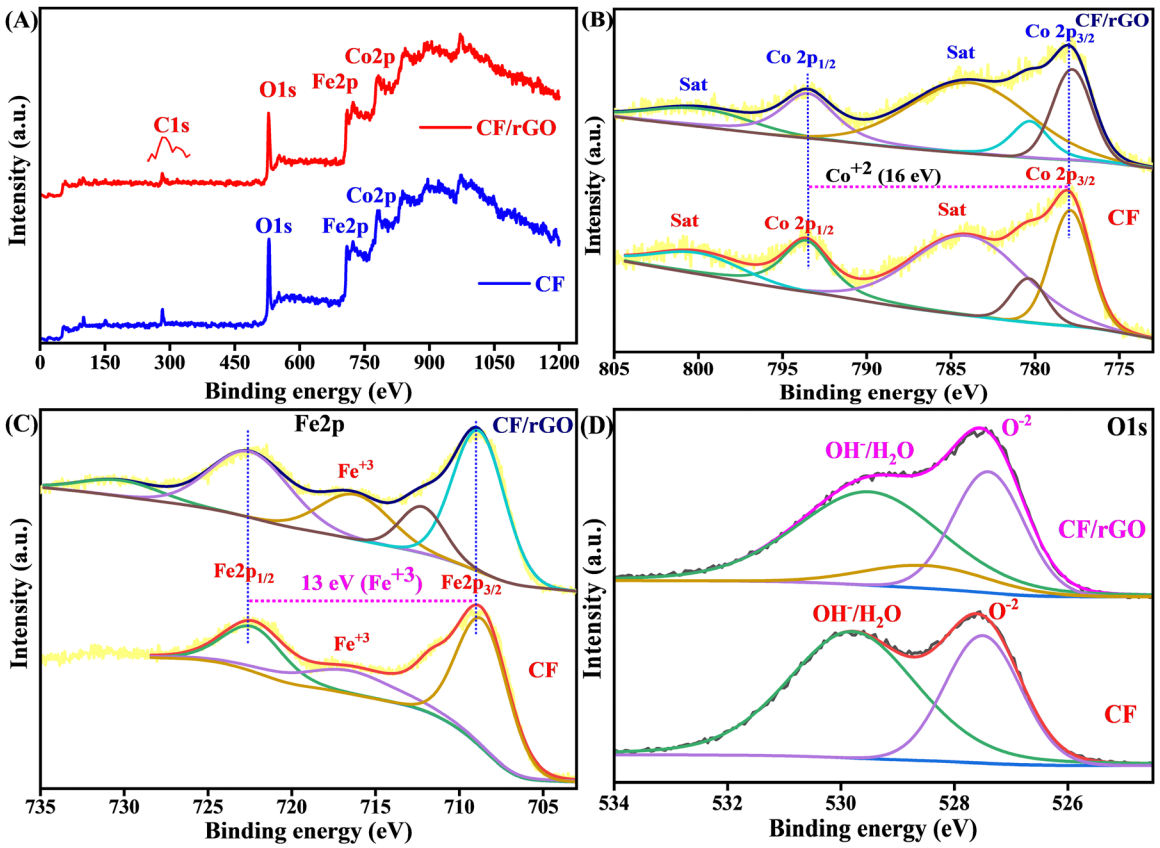

Fig. 5 (A) XPS survey spectra of CF and CF/rGO nh, (B) high-resolution Co 2p XPS fitting peaks, (C) high-resolution Fe 2p XPS fitting peaks with the corresponding oxidation state and binding energy, and (D) binding energy of the O 1s high-resolution XPS peaks.

practical unification of rGO and CF. The high-resolution peak fitting is investigated using the XPS-peak-41 software by applying the Shirley background in each element's XPS analysis. The deconvoluted high-resolution peak of the C 1s spectrum shows binding energies at 282.5–284.1 (C–C/C═C), 285.7 (C–O), and 291 (C═O) eV, respectively, as shown in Fig. S3 (ESI†). The carbon atom in the GO lattice C–C/C═C signifies the sp^2 hybridization, and other residual components signify the oxygen-containing entity in the rGO. Furthermore, the linear fitting background applied in the high-resolution fitted peak of Co 2p at 778 and 793.5 eV correspond to Co $2p_{3/2}$ and Co $2p_{1/2}$ and other satellite peaks at 780.4, 784.1, and 800.3 eV to describe the appearance of the Co^{2+} state. At the same time, the spin–orbit splitting gap is 16 eV to confirm the Co^{2+}

oxidation state[57] in the prepared material, as shown in Fig. 5B. In addition, the Shirley fitted Fe 2p spectrum gives two significant peaks at 722.6 Fe $2p_{1/2}$, and 709.2 Fe $2p_{3/2}$, eV, which confirms the Fe^{3+} state and the peak difference of 13 eV again validates the result of the Fe^{3+} state expressed in Fig. 5C. The Fe^{3+} in O_h and T_d sites are responsible for the first and second fit peaks in spinel ferrites. Some other additional satellite peaks at 712.6 and 716.3 support the Fe^{3+} oxidation state.[19] Fig. 5D expresses the deconvoluted O 1s peak at 527.5 eV for O^{-2}, 528.6 eV for a metal oxygen bond, and 529.7 eV for chemically adsorbed OH/H_2O species in the XPS spectrum. The spin orbit splitting of 16 eV and the triplet and singlet state energy difference of 13 eV signifies the presence of Fe^{3+} and Co^{2+} states respectively. Therefore, the results of the XPS study validate the results of the Raman and XRD analyses and confirm the elemental oxidation state of the hydrothermally synthesized nh ferrite material.

Electrode functionalization, fabrication, laccase immobilization, optimized electrochemical parameters (OEP), and analyte optimization

The functionalized ITO electrode surface (functionalization of the ITO coated glass sheet is discussed in Section S2.1, ESI†) was fabricated by the EPD (instrument model Genetix GX300C) of CF and CF/rGO nh materials. The 12 ml Milli-Q water and 3 ml ethanol mixture containing 25 mg of nanopowder of mesoporous CF and CF/rGO nh EPD solution was prepared after 45 minutes of ultra-sonication, then EPD techniques were used to optimize the applied potential of 25 V for 20 s for deposition. A thin, uniform deposited layer was formed on the functionalized ITO surface using copper as the anode reference electrode and ITO as a cathode electrode. After EPD, the fabricated electrodes CF/ITO and CF/rGO/ITO were washed with Milli-Q water (resistivity 15 Ω sq^{-1}), dried, and stored at 4 °C for later electrochemical analysis.

The biosensing efficiency of the enzyme depends on the surface attachment of biomolecules and the selection of a suitable pH. This allows it to interact electrostatically with oppositely charged (net positive or negative charges of biomolecule) functional groups or surfaces, resulting in enhanced binding affinity, selectivity, and sensitivity of the engineered biosensors. After that, the enzyme immobilization on a CF/rGO/ITO-modified electrode is performed using the drop cast method. Fig. 6A shows the different volumes of enzyme loading used to optimize the R_{ct} response by using the 2, 5, 10, 15, and 20 μl solution of phosphate buffer at pH 7.0. As a result, the 5 μl solutions on the electrode surface have the lowest R_{ct} value (197 Ω), showing the maximum current response, which is a suitable amount of enzyme to use in AD detection. The optimized La enzyme 5 μl solutions are uniformly spread out over an EPD-deposited CF/rGO/ITO electrode surface and dried overnight at room temperature for later investigations. The proposed bioelectrode La/CF/rGO/ITO is ready for further electrochemical CV and EIS analysis (CorrTest CS-350 electrochemical workstation) and stored at 4 °C.

The electrochemical characteristics of the electrodes such as ITO, CF/ITO, CF/rGO/ITO, and La/CF/rGO/ITO bioelectrodes employed in 50 mM phosphate buffer containing NaCl (0.9%), pH 6.5, ferricferro–hexacyano redox couple 5 mM, scan rate 50 mV s^{-1} and optimized potential range is −0.7 to 1 Volt (V) in CV analysis. After that, this reaction condition was also useful in EIS analysis with a frequency range of 100 000 to 0.01 Hz (from initial to final), point/decade is 10, AC amplitude of 5 mV, and effective surface area of La/CF/rGO/ITO bioelectrode is 0.97 cm^2 (calculated by using Randles–Sevcik eqn (S1) discussed in Section S2.1, ESI†). These CV and EIS-optimized electrochemical parameters are jointly denoted as OEP, and utilized in the whole electrochemical analysis.

The standard stoke solution of analyte can be prepared using the AD powder used to prepare 0.2 M concentrated solution in Milli-Q water (resistivity 15 Ω sq^{-1}), then serial dilution to prepare the different micromolar concentrations in 1 ml. After that, the real sample (BSA) was prepared at 50 mg ml^{-1} in a phosphate buffer at neutral conditions by using the standard addition method. Additionally, this BSA solution was further diluted in multiples of 5, 10, 15, and 20, which were used in optimization analysis as shown in Fig. S4 (A and B) (ESI†). The lowest R_{ct} value of the pure BSA (not diluted) was 245 Ω, used as a real sample to prepare a spike solution for AD monitoring.

Electrochemical behavior of the nanofabricated bioelectrode

The CV was used to analyze the current response of an oxidation–reduction reaction based on the applied potential to measure the current response, which can be found in the ESI† in Fig. S5 (Section S2.2). At the same time, EIS was used to evaluate the electrochemical impedance of a system across various frequencies for a specific alternating current pulse. Nyquist plots of ITO, CF/ITO, CF/rGO/ITO, and La/CF/rGO/ITO bioelectrodes were used to assess impedance changes resulting from the modifications made to the electrode surfaces shown in Fig. 6B. In these plots, the linear part at low frequencies (close to 45° angle) is the diffusion-limiting process. In contrast, the semicircular segment in the high frequencies zone specified the electron-transfer restrictions in the electrochemical EIS analysis. The intersection of the Nyquist plot with the *X*-axis represents the total series resistance (R_s) of the electrode, including connecting wires and instrument circuitry. The values of series resistance for the four electrodes ITO, CF/ITO, CF/rGO/ITO, and La/CF/rGO/ITO are identical (58 Ω), reflecting the total series resistance of the circuit, which includes wire and cell response resistances.

The EIS data were fitted using an appropriate model resembling the sensor circuit, yielding values for R_s, charge transfer resistance (R_{ct}), and Warburg short (Ws) as the diffusion resistance. The R_{ct} values for ITO, (374 Ω), CF/ITO (307 Ω), CF/rGO/ITO (250 Ω), and La/CF/rGO/ITO (194 Ω) electrodes were observed at OEP, sequentially. The integration of rGO nanosheets in the nh electrode increased its electronic conductivity, and electron-transfer process, as indicated by the reduced R_{ct} value of 250 Ω for the CF/rGO/ITO electrode. Interestingly, the La/CF/rGO/ITO electrode displayed a significantly lower charge-transfer resistance (194 Ω) compared to the

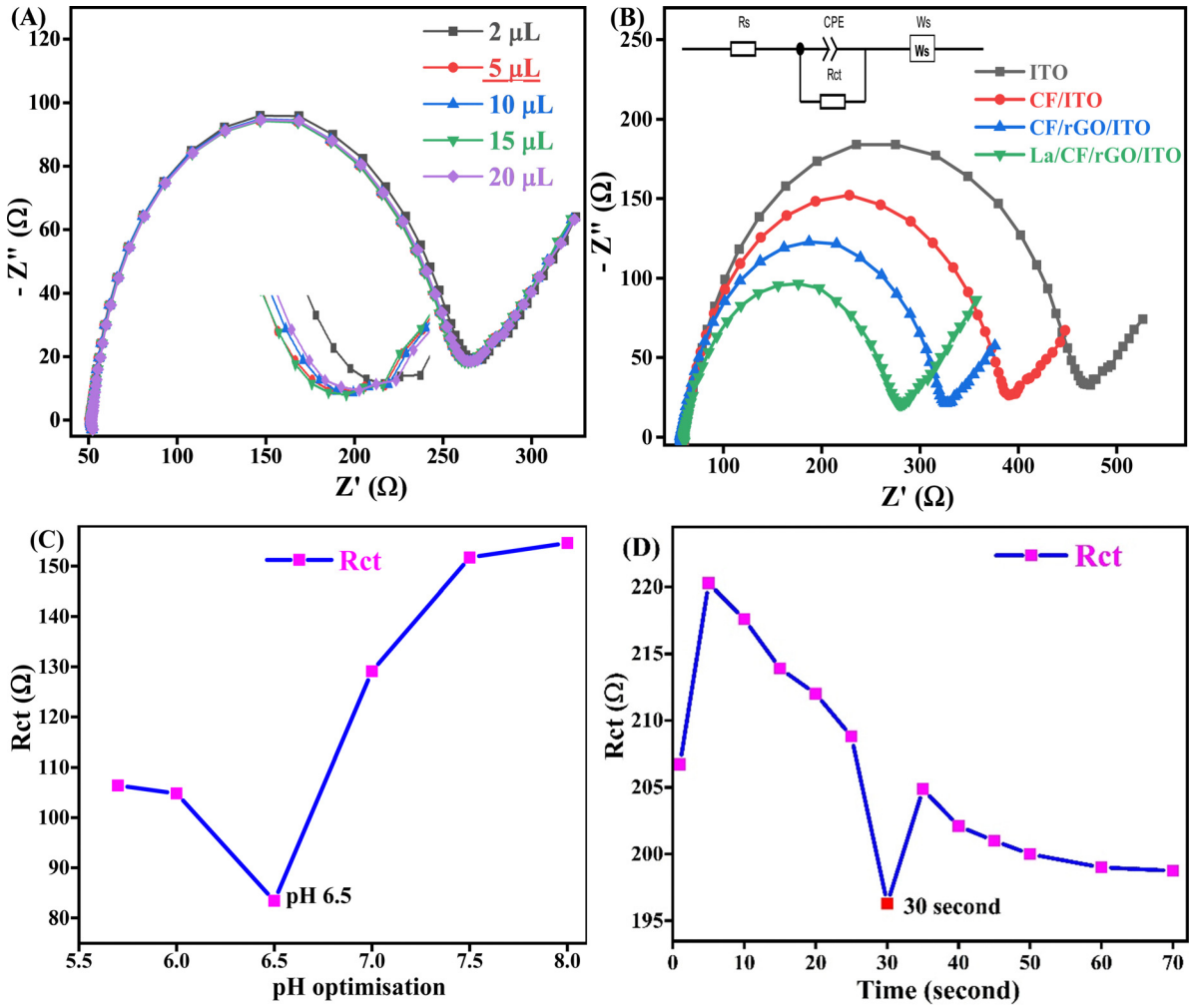

Fig. 6 (A) Nyquist plot of optimization of laccase immobilization on the fabricated CF/rGO/ITO electrodes, (B) EIS spectra of the Nyquist plot of the ITO, CF/ITO, CF/rGO/ITO, and La/CF/rGO/ITO electrodes presented in Ohm, (C) optimisation of the pH for effective interactions in phosphate buffer electrolyte, and (D) the response time analysis on the enzymatic bioelectrode.

others, suggesting an efficient electron conductive channel towards the bioelectrode for the current generation and significant interaction between the bioelectrode and analyte. The Randles circuit model was used to estimate the R_{ct} values for all four electrodes, including the biosensor. Moreover, for the La/CF/rGO/ITO electrode, the R_{ct} value was employed to calculate the heterogeneous charge transfer rate constant[19] (K_s) for the redox couple by using eqn (5).[58] The K_s value for the fabricated electrode ITO (1.47×10^{-4} s^{-1}), CF/ITO (1.79×10^{-4} s^{-1}), CF/rGO/ITO (2.19×10^{-4} s^{-1}), and La/CF/rGO/ITO (2.83×10^{-4} s^{-1}), respectively. The CV and EIS result shows that the prepared bioelectrode La/CF/rGO/ITO is suitable for the electrochemical monitoring of AD.

$$K_s = RT/n^2F^2AR_{ct}C \quad (5)$$

Here R is 8.314 J mol^{-1} K^{-1} the gas constant, T = 300 Kelvin, F is the Faraday constant (96 500 C mol^{-1}), n is the number of electrons involved, A is the effective surface area, and C is the concentration of electrolyte (5×10^{-6} mol cm^{-3}).

The pH level of its environment significantly influenced the electrical response of the enzyme–substrate interface. Specifically, the La enzyme showed an optimal pH range between 5.5 and 8.0, neutral to slightly basic. This pH range was crucial for effective interaction for enzyme–substrate binding. Additionally, variations in pH affected the AD binding to the enzyme and the K_s at the electrode surface. Extreme pH conditions, either highly acidic or alkaline, could cause degradation or corrosion of the electrode surfaces, compromising biosensor reliability. To better understand and optimize these pH effects, an experiment was conducted using a La/CF/rGO/ITO bioelectrode in a range of pH solutions (from 5.7–8.0) at an OEP. The results, displayed in Fig. 6C, highlighted the profound impact of pH on the R_{ct} value. It was observed that at higher pH, the peak potential shifted a little toward the positive side. The peak current rose with an increase up to a pH value of 7.5 at 150 Ω and the R_{ct} value reached saturation as the pH rose to 8.0. There is a line parallel to the X-axis, as seen between pH 5.7 and 6.0, so the optimum pH range could be 6.5 (lowest R_{ct} value), which is close to neutral pH. Therefore, a pH of 6.5 was identified as

the most effective interaction for AD monitoring, yielding a low R_{ct} value (high electrical conductivity). Researchers must meticulously regulate and optimize the pH conditions during biosensing experiments for accurate and reliable AD detection.

The EIS technique used in response time analysis was performed in the range of 1–70 s with 5 s intervals taken after completing the analysis at OEP, using AD (100 μM, 50 μl) in phosphate buffer on the proposed La/CF/rGO/ITO bioelectrode. Thus, the maximum electrical conductivity was achieved at 30 s, which means the R_{ct} value at this point was found to be the lowest (196 Ω) in the Nyquist plot shown in Fig. 6D. Additionally, the proposed biosensors are reliable for monitoring neurotransmitters, and 30 s response time is good for biosensing applications of standard and real sample detection of AD.

The kinetic analysis and scan rate effects of the nanofabricated La/CF/rGO/ITO electrode were investigated from 10 to 100 mV s^{-1} with regular intervals of 10 mV s^{-1}, as shown in Fig. S6(A) (ESI†). The scan rate steps follow the increase of anodic/oxidation current peak (I_{pa}) and cathodic/reduction current peak (I_{pc}) due to the decrease of diffusion layer with increasing scan rate, resulting in the mass transfer process/diffusion-controlled process, and quasi-reversible nature of the bioelectrode. Fig. S6(B) (ESI†) shows the linear calibration graph between the square root of the scan rate ($\nu^{1/2}$) *versus* current (mA), which is used to calculate the kinetic parameters such as surface concentration (I^*), effective surface area, and diffusion coefficient (D) discussed in the ESI† as eqn (S2) and (S3) (Section S2.2).

It has been investigated how the concentration of particular analytes in solutions relates to the impedance. The total R_s is calculated below.

$$R_s = R_{solution} + R_d + R_{circuit+instrument}$$

Here, R_s is the total series resistance of the circuit, that is, the linear sum of $R_{solution}$, R_d, and $R_{circuit+instrument}$; terms have their self-explanatory meanings as solution resistance, diffusion resistance, and total circuit resistance present in the system, including connecting wires, respectively. The voltammograms are slightly sloped, indicative of constant phase element (CPE) behavior, which cannot be ascribed to the ohmic drop. This CPE behavior stems from a distribution of time constants, explained by the dispersion of the interfacial capacitance and solution resistance. The analysis of the capacitive current reveals nonlinear behavior consistent with a CPE highlighting the necessity of incorporating a CPE element for a realistic description of the interface. Omitting this element could lead to significant errors in capacity determination. While an ideal capacitor is expected to exhibit purely non-faradaic behavior and shift electric signals by a phase of π/2, practical observations show non-ideal behavior, with phase shifts of n·π/2, where n typically ranges from about 0.8 to 1. Due to this phase shift variation, the element is termed a CPE, which also encompasses a standard capacitor when n equals 1. Its impedance is expressed below[59]

$$Z_{CPE} = \frac{1}{Y_0(i\omega)^n}$$

Y_0 and n are characteristic parameters of CPE. Here, n ($0 \leq < n \leq 1$) is an independent parameter; if $n = 1$, CPE becomes a geometrical pure capacitor. A CPE results in a better fitting curve than a capacitor, but its parameter Y_0 does not give any relevant physical significance as the capacitor does. To convert Y_0 into equivalent capacitance[60]

$$C = \frac{Y_0(\omega)^n}{\sin(n\pi/2)}$$

To make it worthwhile for practical application for real systems, many scientists have suggested an advanced conversion method with ω'_{max} as the frequency where the imaginary part of impedance has its maximum, as follows[61]

$$C = Y_0(\omega'_{max})^{n-1}$$

The La/CF/rGO/ITO bioelectrode demonstrates a high affinity for the analyte AD, exhibiting a sensitivity of 0.214 Ω μM^{-1} cm^{-2}. The bioelectrode can detect AD across a longer linearity of 1 to 500 μM than reported in previously published articles,[1,62] as shown in Fig. 7A. The La/CF/rGO/ITO bioelectrode in detecting varying concentrations of AD was evaluated using the R_{ct} values obtained from EIS measurements spanning a frequency range from 100 000–0.1 Hz, with a stimulus of 5 mV at the OEP. The R_{ct} values, determined after fitting the data to an appropriate model as depicted in Fig. 7B (inset), served to assess the bioelectrode's response to different AD concentrations. A Nyquist plot shows the R_{ct} values ranging from 360 Ω to 250 Ω across different AD concentrations, indicating a linear decrease in R_{ct} value with increasing AD concentration. This linear relationship is further supported by following the equation $y(R_{ct}) = -0.208x$ (μM) + 348.6 and linear regression coefficient (R^2) of 0.98, which underpins the calibration of the fabricated biosensor as shown in Fig. 7B. The limits of detection [LoD = 3 × SD/sensitivity], and quantification [LoQ = 10 × SD/sensitivity], were calculated based on a signal-to-noise ratio (s/n = 3), resulting in values of 40.3 μM LoD and 134.5 μM, LoQ, respectively, with a sensitivity of 0.214 Ω Mm^{-1} cm^{-2}.

The decrease in R_{ct} value with increasing AD concentration is attributed to the higher availability of AD biomolecules for interaction with the bioelectrode surface (more active sites and surface area available), which is enhanced by the nh's high surface area (119.2 m^2 g^{-1}) confirmed by BET analysis. These electrostatic interactions (positive charge on metal ions and negatively charged oxygen-containing analyte on the electrode surface) facilitate conductive pathways for electron transfer, reducing R_{ct} and improving charge transfer efficiency. The high electrical conductivity and more binding sites at the fabricated bioelectrode interface (La and nh) are the causes of this effect. The sensitive diagnosis of AD *via* EIS is made possible by these specific advantages. The synergistic effect between the La enzyme and mesoporous CF/rGO nh, and the effective electrochemical reaction of AD at the bioelectrode surface are shown in Scheme 1. This nh boosts electrochemical performance by creating a conductive microenvironment, La facilitates

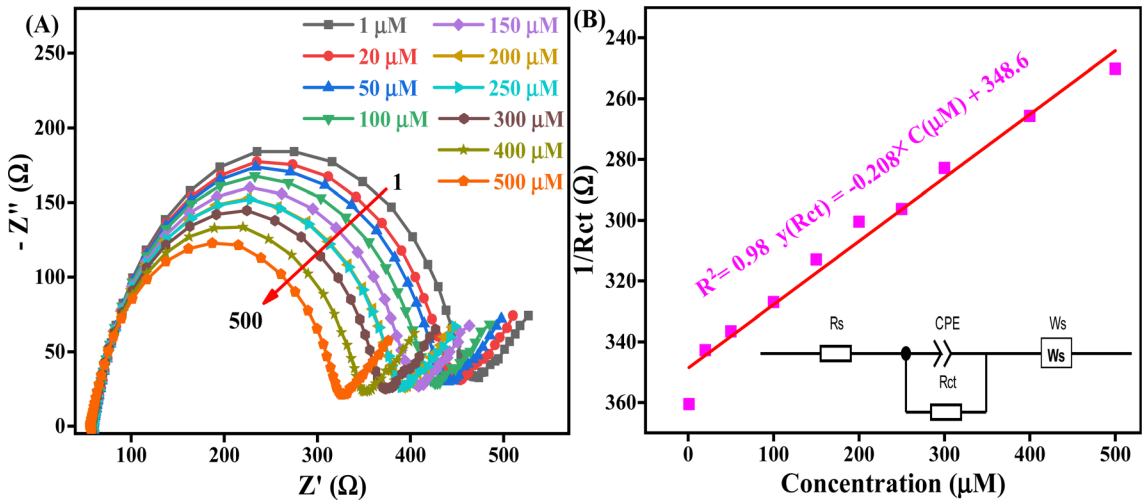

Fig. 7 (A) EIS spectra of the Nyquist plot on the nanofabricated La/CF/rGO/ITO bioelectrode from 1 to 500 μM, expressed in Ohm, and (B) biosensing linear calibration curve of AD, expressed in between the $1/R_{ct}$ *versus* different concentrations of AD at OEP, and the inset shows the equivalent circuit.

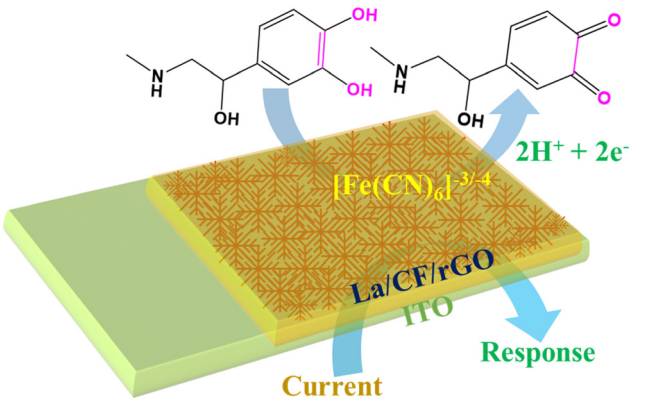

Scheme 1 The electrochemical mechanism of the biosensor on the fabricated electrode.

charge transfer and the bioelectrode improves the electrode's surface area and electronic conductivity for AD oxidation. Effective electrocatalysis and variations in EIS parameters result from these interactions, making it possible to quantify and analyze AD concentrations. This has great potential for use in healthcare monitoring and diagnostics.

The reusability of the proposed AD biosensor was evaluated through 14 consecutive tests conducted in a 10 ml phosphate buffer, which included 50 μl of an 80 μM AD solution at OEP. The R_{ct} value consistently recorded was 210 ± 4 Ω, with less than 3.16% relative standard deviation (RSD). Furthermore, the high reusability of the fabricated bioelectrode is due to the effective interaction between the La/CF/rGO/ITO bioelectrode and the La enzyme present on the electrode surface. This demonstrates the biosensor's capacity for repeated use, as evidenced by the data presented in Fig. 8A, which confirms the reusability of the prepared biosensor is excellent (In14 days, RSD 0.40%) for AD monitoring.

The stability study of the biosensor is crucial for reliable sensing devices. The stability of the prepared La/CF/rGO/ITO bioelectrode is demonstrated by utilizing the R_{ct} value for up to 1–70 days, by a regular interval of five days at OEP. As a result of the stability investigation, it was concluded that the % RSD ranged from 0 to 9.9% for 1 to 70 days, as presented in Fig. 8B. After 70 days, the % RSD is more than 10%, which confirmed that the fabricated bioelectrode La/CF/rGO/ITO is stable because the CF and rGO on the electrode surface provides a solid electrostatic interaction for metal ions with oxygen-containing rGO in the electrolytic solutions. It has been found that the bioconjugated electrode is stable for up to 70 days in 80 μM (50 μl) AD solution at OEP. Thus, the EIS-based biosensor demonstrated good reusability and stability of the fabricated La/CF/rGO/ITO bioelectrode for monitoring AD neurotransmitters.

All the EIS studies were performed at pH 6.5 to detect AD. Fig. 8C shows a selectivity study of the fabricated biosensor towards AD by using the EIS technique in the presence of potential interfering analytes uric acid, dopamine, glutamic acid, urea, ascorbic acid, glucose, and lactic acid. The standard solution used in the selectivity test is 80 μM of each and 50 μl volume to investigate the analysis using the OEP. The biosensor response showed a % RSD change from 1.25 to 5.8% in the presence of these interfering analytes. These results signify the nanofabricated La/CF/rGO/ITO bioelectrode is highly selective, stable, reproducible, and practically viable for real sample monitoring of AD neurotransmitters. Thus, the CF/rGO nh is a reliable platform for detecting AD in the presence of various interfering analytes.

Under the same reaction conditions, EIS techniques were used to investigate the spiked BSA real sample with the standard AD analytes. Six distinct AD concentrations, namely 5, 10, 20, 40, 60, and 80 μM, were tested for spike-specified concentrations of AD in a fetal BSA solution in phosphate buffer at pH 6.5 in OEP. Fig. 8D displays the R_{ct} response in the standard and BSA serum samples. Furthermore, Table 1 shows that standard and real BSA spike samples recovered at greater than the spiked concentrations and RSD below 8.3%. As a result, the EIS-based responses of the standard AD sample and the serum sample (spike BSA real samples) correspond well, and the CF/rGO nh was

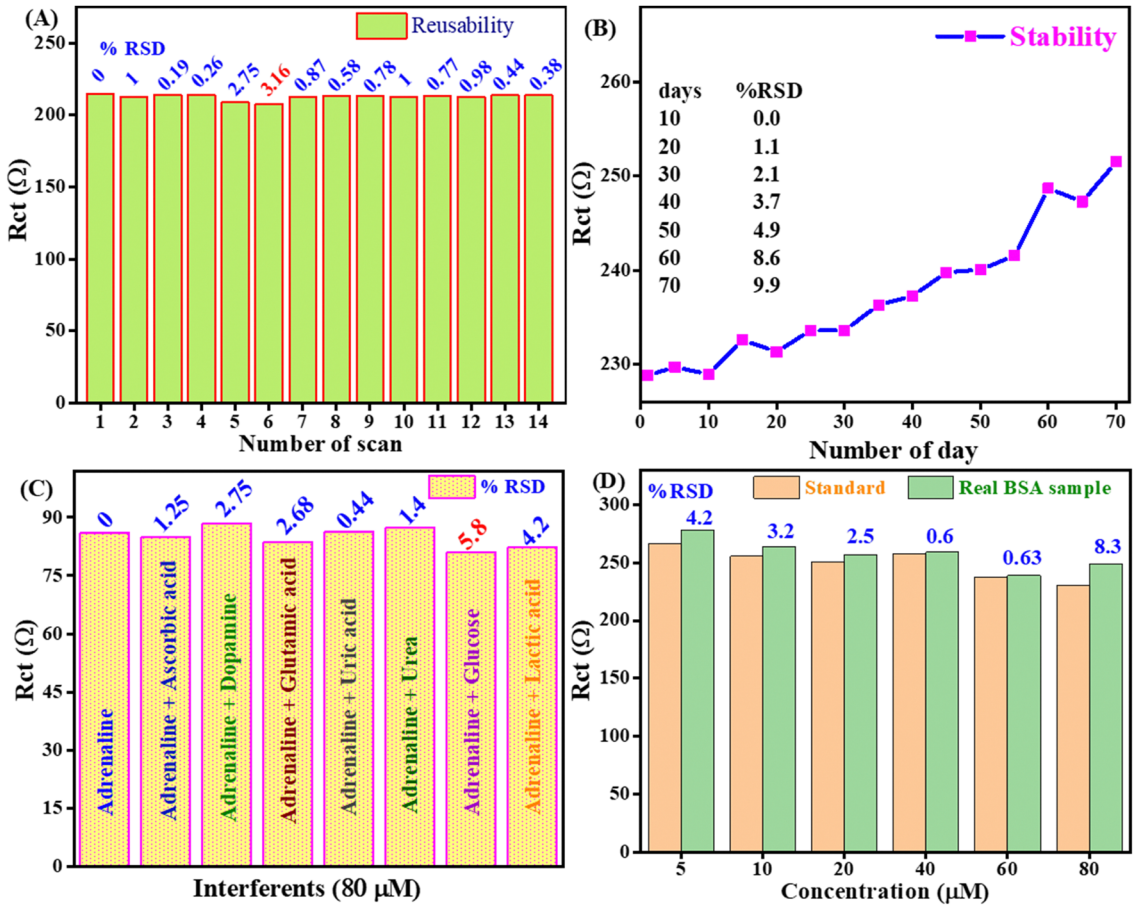

Fig. 8 (A) and (B) The reusability and stability of the fabricated La/CF/rGO/ITO, with % RSD. (C) Selectivity behavior of the fabricated bioelectrode in the presence of interfering analytes with % RSD by interference analysis, and (D) different concentrations of real BSA spike samples and AD known sample comparative analysis with % RSD.

Table 1 AD concentration detection in real spiked BSA samples by applying the standard addition method

Standard AD concentration added (μM) in BSA	Concentration determined in real BSA samples (μM)	Recovery (%)	RSD (%)
5	5.2	104	4
10	10.3	103	3
20	20.51	102.5	2.5
40	40.27	100.6	0.6
60	60.3	100.5	0.5
80	86.7	108.3	8.3

determined to be a superior material for AD biosensors in an enzymatic environment. Thus, the prepared biosensor is reliable for the selective monitoring of AD in real samples and important for neurodegenerative disorders.

Conclusion

In this work, we focussed on hydrothermally synthesized mesoporous CF and CF/rGO nh and successfully established the monitoring of neurotransmitters. Physicochemical characterization such as XRD, Raman UV-visible, FTIR, HR-TEM, and BET revealed the formed mesoporous CF/rGO nh. The nanofabricated La/CF/rGO/ITO bioelectrode shows that the synergic combination of rGO and CF provides an excellent platform for impedimetric AD detection. The BET analysis confirms the mesoporous nature, large surface area for enzyme loading, and effective interaction with analytes. Furthermore, a high rate of K_s was obtained for the La-conjugated interface. The strain in CF reflects the Fermi level tailoring that leads to faster charge transfer, and porosity providing a larger surface area for the analyte to work with. The presence of CPE in the equivalent circuit model reflects the significant porosity, providing a surface for AD interaction. The EIS-optimized parameters based on R_{ct} demonstrated excellent performance in terms of stability, reusability (14 times), longer linearity 1–500 μM, high sensitivity (0.214 Ω μM^{-1} cm^{-2}), good selectivity (below 5.8% RSD), and reliability for real BSA spike samples analysis. This suggests a potential application of the CF/rGO nh material in enzymatic monitoring of AD neurotransmitters, and is beneficial for managing neurodegenerative disorders and diseases.

Author contributions

R. V.: data curation, investigation, data validation, visualization, EIS data fitting, and writing – original draft. S. K. Y.: data curation,

EIS experiment setup, equivalent circuit modeling, visualization, and writing – review & editing of the original draft. D. S.: review & editing of the original draft. J. S.: conceptualization, validation, project administration, resources, supervision, and writing – review & editing of the original draft.

Data availability

The data supporting this study's findings are available on request from the corresponding author, Jay Singh, email: **https://jaysingh.chem@bhu.ac.in**. The data are not publicly available due to privacy reasons.

Conflicts of interest

The authors declare that they have no known competing financial interests or personal relationships that could have appeared to influence the work reported in this paper.

Acknowledgements

This work received no specific grant from public, commercial, or not-for-profit funding agencies. R. V. is thankful to his affiliated institution for providing constant financial support. S. K. Y. is thankful to BHU for IoE MPDF Award number 55770 and J. S. acknowledges BHU for providing an additional seed grant and BRIDGE grant under MoE Govt. India, Institute of Eminence (IoE), under Dev. Scheme No. 6031 & 6031A respectively.

References

1 S. Kumar, A. Awasthi, M. D. Sharma, K. Singh and D. Singh, *Mater. Chem. Phys.*, 2022, **290**, 126656.
2 A. Bhattacharya, K. B. Patel, R. Ghosh, D. N. Srivastava and P. B. Chatterjee, *Sens. Actuators, B*, 2024, **398**, 134772.
3 S. S. Shankar, R. M. Shereema and R. B. Rakhi, *ACS Appl. Mater. Interfaces*, 2018, **10**, 43343–43351.
4 M. Mukhopadhyay, A. Banerjee, R. Majumder, A. Chattopadhyay and D. Bandyopadhyay, *Adv. Redox Res.*, 2024, **11**, 100101.
5 B. Mekassa, M. Tessema, B. S. Chandravanshi, P. G. L. Baker and F. N. Muya, *J. Electroanal. Chem.*, 2017, **807**, 145–153.
6 C. Pimentel, L. Batista-Nascimento, C. Rodrigues-Pousada and R. A. Menezes, *Oxid. Med. Cell. Longevity*, 2012, **2012**, 1–9.
7 K. Chetankumar, B. E. Kumara Swamy and S. C. Sharma, *Microchem. J.*, 2021, **160**, 105729.
8 N. Alizadeh, S. Ghasemi, A. Salimi, T.-K. Sham and R. Hallaj, *Colloids Surf., B*, 2020, **195**, 111228.
9 P. Oeckl, P. Steinacker, C. A. F. von Arnim, S. Straub, M. Nagl, E. Feneberg, J. H. Weishaupt, A. C. Ludolph and M. Otto, *J. Proteome Res.*, 2014, **13**, 4518–4525.
10 G. Kaluza, *Calm and Confident Under Stress*, Springer Berlin Heidelberg, Berlin, Heidelberg, 2022, pp. 17–44.
11 E. Stump, *Neurol. Today*, 2007, **7**, 25.
12 S. Sharma, N. Singh, V. Tomar and R. Chandra, *Biosens. Bioelectron.*, 2018, **107**, 76–93.
13 H. Kaur, S. S. Siwal, R. V. Saini, N. Singh and V. K. Thakur, *ACS Nanosci. Au*, 2023, **3**, 1–27.
14 X. Ling, R. Shi, J. Zhang, D. Liu, M. Weng, C. Zhang, M. Lu, X. Xie, L. Huang and W. Huang, *ACS Sens.*, 2018, **3**, 1683–1689.
15 S. Dutta, C. Ray, S. Mallick, S. Sarkar, R. Sahoo, Y. Negishi and T. Pal, *J. Phys. Chem. C*, 2015, **119**, 23790–23800.
16 P. Pantiya, B. P. Guiard and G. Gotti, *Chromatographia*, 2024, **87**, 175–185.
17 Asmaa H. Abbas, T. N. Al-Sabha and S. M. J. Al-Mtwaiti, *J. Anal. Chem.*, 2024, **79**, 784–797.
18 D. Maity, S. R. Sahoo and S. Saha, Synthesis and characterization of nanomaterials for electrochemical sensors, in *Recent Developments in Green Electrochemical Sensors: Design, Performance, and Applications*, American Chemical Society, 2023, pp. 193–222.
19 R. Verma, S. K. Yadav, K. R. Singh, R. Verma, D. Kumar and J. Singh, *ACS Appl. Bio Mater.*, 2023, **6**, 5842–5853.
20 M. A. M. Khan, W. Khan, M. Ahamed, J. Ahmed, M. A. Al-Gawati and A. N. Alhazaa, *ACS Omega*, 2020, **5**, 31076–31084.
21 D. Chen, H. Feng and J. Li, *Chem. Rev.*, 2012, **112**, 6027–6053.
22 A. Ambrosi, C. K. Chua, A. Bonanni and M. Pumera, *Chem. Rev.*, 2014, **114**, 7150–7188.
23 W. Luo and S. Zafeiratos, *ChemCatChem*, 2017, **9**, 2432–2442.
24 A. Mondal, A. Prabhakaran, S. Gupta and V. R. Subramanian, *ACS Omega*, 2021, **6**, 8734–8743.
25 Z. Wu, S. Bai, J. Xiang, Z. Yuan, Y. Yang, W. Cui, X. Gao, Z. Liu, Y. Jin and B. Sun, *Nanoscale*, 2014, **6**, 10505–10510.
26 M. Arivazhagan, B. Mohan and J. Jakmunee, *Green Anal. Chem.*, 2024, **10**, 100127.
27 R. Verma, K. R. Singh, R. Verma, R. P. Singh and J. Singh, *New J. Chem.*, 2024, **48**, 554–568.
28 S. Wu, Q. He, C. Tan, Y. Wang and H. Zhang, *Small*, 2013, **9**, 1160–1172.
29 M. Ghasemlou, F. Daver, E. P. Ivanova, Y. Habibi and B. Adhikari, *Prog. Polym. Sci.*, 2021, **119**, 101418.
30 N.-F. Chiu, S.-Y. Fan, C.-D. Yang and T.-Y. Huang, *Biosens. Bioelectron.*, 2017, **89**, 370–376.
31 R. Verma, K. R. Singh, R. Verma and J. Singh, *RSC Appl. Interfaces*, 2024, **1**, 252–267.
32 R. Sivasubramanian and P. Biji, *Mater. Sci. Eng. B*, 2016, **210**, 10–18.
33 A. Ahmed, A. Singh, S.-J. Young, V. Gupta, M. Singh and S. Arya, *Composites, Part A*, 2023, **165**, 107373.
34 Y. Wu, D. Li, C.-L. Wu, H. Y. Hwang and Y. Cui, *Nat. Rev. Mater.*, 2022, **8**, 41–53.
35 J. Liu, J. Tang and J. J. Gooding, *J. Mater. Chem.*, 2012, **22**, 12435.
36 P. Balasubramanian, T. S. T. Balamurugan, S.-M. Chen and T.-W. Chen, *J. Hazard. Mater.*, 2019, **361**, 123–133.
37 S. Akbari, S. Jahani, M. M. Foroughi and H. Hassani Nadiki, *RSC Adv.*, 2020, **10**, 38532–38545.
38 M. M. Foroughi, S. Jahani and M. Rajaei, *J. Electrochem. Soc.*, 2019, **166**, B1300–B1311.

39 Z. Fathi, S. Jahani, M. S. Zandi and M. M. Foroughi, *Anal. Bioanal. Chem.*, 2020, **412**, 1011–1024.
40 J. S. Beveridge, J. R. Stephens and M. E. Williams, *Annu. Rev. Anal. Chem.*, 2011, **4**, 251–273.
41 P. R. Solanki, A. Kaushik, V. V. Agrawal and B. D. Malhotra, *NPG Asia Mater.*, 2011, **3**, 17–24.
42 M. Colombo, S. Carregal-Romero, M. F. Casula, L. Gutiérrez, M. P. Morales, I. B. Böhm, J. T. Heverhagen, D. Prosperi and W. J. Parak, *Chem. Soc. Rev.*, 2012, **41**, 4306.
43 R. Verma, K. R. Singh, R. Verma and J. Singh, *Luminescence*, 2023, **38**, 1393–1404.
44 A. Roychoudhury, A. Prateek, S. Basu and S. K. Jha, *J. Nanopart. Res.*, 2018, **20**, 70.
45 W. S. Hummers and R. E. Offeman, *J. Am. Chem. Soc.*, 1958, **80**, 1339.
46 N. Gill, A. L. Sharma, V. Gupta, M. Tomar, O. P. Pandey and D. P. Singh, *J. Alloys Compd.*, 2019, **797**, 1190–1197.
47 J. Singh, A. Roychoudhury, M. Srivastava, V. Chaudhary, R. Prasanna, D. W. Lee, S. H. Lee and B. D. Malhotra, *J. Phys. Chem. C*, 2013, **117**, 8491–8502.
48 K. Alexopoulos, J. Boskovits, S. Mourikis and M. Roilos, *Acta Crystallogr.*, 1965, **19**, 349–353.
49 M. D. Aggarwal and J. K. D. Verma, *Czech. J. Phys.*, 1972, **22**, 621–623.
50 P. Chandramohan, M. P. Srinivasan, S. Velmurugan and S. V. Narasimhan, *J. Solid State Chem.*, 2011, **184**, 89–96.
51 R. S. Diab, L. M. S. El-Deen, M. H. Nasr, A. A. EL-Hamalawy and A. S. Abouhaswa, *J. Mater. Sci.: Mater. Electron.*, 2024, **35**, 290.
52 D. Moitra, C. Anand, B. K. Ghosh, M. Chandel and N. N. Ghosh, *ACS Appl. Energy Mater.*, 2018, **1**, 464–474.
53 M. A. Majeed Khan, R. Siwach, S. Kumar and A. N. Alhazaa, *Opt. Laser Technol.*, 2019, **118**, 170–178.
54 S. A. Ansari, N. Parveen, G. M. Alsulaim, A. A. Ansari, S. A. Alsharif, K. M. Alnahdi, H. A. Alali and V. R. M. Reddy, *Surf. Interfaces*, 2023, **40**, 103078.
55 R. M. Thankachan, M. M. Rahman, I. Sultana, A. M. Glushenkov, S. Thomas, N. Kalarikkal and Y. Chen, *J. Power Sources*, 2015, **282**, 462–470.
56 S. Adhikari, D. Sarkar and G. Madras, *ACS Omega*, 2017, **2**, 4009–4021.
57 K. V. Sankar, S. Shanmugapriya, S. Surendran, S. C. Jun and R. K. Selvan, *J. Colloid Interface Sci.*, 2018, **513**, 480–488.
58 E. P. Randviir, *Electrochim. Acta*, 2018, **286**, 179–186.
59 P. Zoltowski, *J. Electroanal. Chem.*, 1998, **443**, 149–154.
60 E. P. van Westing, G. Ferrari and J. H. de Wit, *Corros. Sci.*, 1993, **34**, 1511–1530.
61 C. H. Hsu and F. Mansfeld, *Corrosion*, 2001, **57**, 747–748.
62 S. D. Sukanya, B. E. K. Swamy, J. K. Shashikumara, S. C. Sharma and S. A. Hariprasad, *Sci. Rep.*, 2023, **13**, 4523.